

**Construction and Verification of Pourbaix Diagrams for CO<sub>2</sub> Corrosion of Mild Steel  
Valid up to 250°C**

T. Tanupabrunsun, D. Young, B. Brown and S. Nešić

Institute for Corrosion and Multiphase Technology, Ohio University,  
342 West State Street, Athens, OH 45701, USA

**ABSTRACT**

The Pourbaix diagrams for an Fe-CO<sub>2</sub>-H<sub>2</sub>O system at elevated temperatures were constructed using thermodynamic theory and data and then correlated with observed CO<sub>2</sub> corrosion phenomena of mild steel up to 250°C. In the range 80-150°C corrosion product layer formed and the surface analysis showed a mixture of crystal morphologies on the steel surfaces, for experiments lasting 4 days. Kinetic studies conducted at 120°C show full transformation from plate-like to oblong prismatic crystals over 30 days. No obvious crystal morphology was identified on the surfaces of samples studied at 200°C and 250°C. XRD analysis indicates that FeCO<sub>3</sub> and Fe<sub>2</sub>(OH)<sub>2</sub>CO<sub>3</sub> formed on the steel surface at 80-150°C. At 200-250°C, the corrosion product was exclusively Fe<sub>3</sub>O<sub>4</sub>. With surface pH consideration, the generated Pourbaix diagrams were validated by the experimental results. Maximum weight loss corrosion rates were observed at 120°C.

Keywords: Pourbaix diagram, CO<sub>2</sub> corrosion, elevated temperature, mild steel

**INTRODUCTION**

CO<sub>2</sub> corrosion in the oil and gas industry has been widely investigated. Nevertheless, research on CO<sub>2</sub> corrosion at elevated temperatures has rarely been conducted; consequently, the corrosion mechanisms remain unclear. One of the important factors in CO<sub>2</sub> corrosion phenomena is the morphology and identity of corrosion products. Some previous research has indicated the effect of temperature on the CO<sub>2</sub> corrosion product layers to be as follows:

- At temperatures lower than 60°C, no corrosion product layer is formed.<sup>1-3</sup>
- At temperatures greater than 60°C, Fe<sub>2</sub>(OH)<sub>2</sub>CO<sub>3</sub> was detected in the corrosion product layer.<sup>4</sup>
- At 100°C, trace amounts of Fe<sub>3</sub>O<sub>4</sub>/Fe(OH)<sub>2</sub> were observed in the FeCO<sub>3</sub> dominant scale.<sup>5</sup>
- At temperatures between 60°C and 130°C pitting corrosion occurs and the scale consists of thick, prismatic crystals of FeCO<sub>3</sub>.<sup>6-9</sup>
- At temperatures between 130°C and 200°C, the fine grained, dense, adherent scale that has been observed is composed of FeCO<sub>3</sub> and Fe<sub>3</sub>O<sub>4</sub>.

- At temperatures 20°C to 40°C, additional more complex carbonate compounds, including  $\text{Fe}_2(\text{OH})_2\text{CO}_3$ ,  $\text{Fe}_6(\text{OH})_{12}\text{CO}_3$ ,  $\text{Fe}_6(\text{OH})_{12}\text{CO}_3 \cdot \text{H}_2\text{O}$  and  $\text{Fe}_2\text{O}_2\text{CO}_3$ , have been proposed to form as corrosion products.<sup>10</sup>

As indicated above by the few key studies listed, many questions and uncertainties surround the corrosion product layer formation in  $\text{CO}_2$  corrosion of mild steel at high temperatures. This ambiguity in the open literature indicates that more research needs to be done in order to elucidate the nature of corrosion products formed in  $\text{CO}_2$  corrosion of mild steel in the temperature range of 25-250°C.

The potential-pH, or Pourbaix, diagram is a well-known tool for predicting the most stable corrosion product using thermodynamic theory. The Pourbaix diagrams for metal-water systems at 25°C have been established for various metals in the *Atlas of Electrochemical Equilibria in Aqueous Solutions*.<sup>11</sup> Some authors have developed Pourbaix diagrams for an Fe-H<sub>2</sub>O system at elevated temperatures with Fe,  $\text{Fe}^{2+}$ ,  $\text{Fe}_3\text{O}_4$ ,  $\text{Fe}(\text{OH})_2$ ,  $\text{Fe}_2\text{O}_3$  and  $\text{FeO}(\text{OH})$  considered as the most stable species.<sup>12-16</sup> Many extensions of the basic Pourbaix diagrams for a Fe-H<sub>2</sub>O system that include  $\text{CO}_2$  are available freely and as commercial software packages. They can predict the most stable iron species for a bicarbonate/carbonate ( $\text{HCO}_3^-/\text{CO}_3^{2-}$ ) aqueous system by using a specified concentration of  $\text{HCO}_3^-$  and then cover the full range of pH. However, this does not directly relate to a practical system where one typically has a constant aqueous concentration of dissolved  $\text{CO}_2$ , rather than a constant  $\text{HCO}_3^-$  concentration. When a corrosion engineer is interested in the effect of  $\text{CO}_2$  on corrosion of mild steel, the aqueous concentration of  $\text{CO}_2$  is assumed to be constant and can be easily calculated as a function of temperature and partial pressure of  $\text{CO}_2$ . When considering the equilibrium state of a  $\text{CO}_2$  system, the concentrations of  $\text{HCO}_3^-/\text{CO}_3^{2-}$  will vary widely with pH, for a constant concentration of dissolved  $\text{CO}_2$ . Therefore, in this research the potential-pH diagrams for an Fe- $\text{CO}_2$ -H<sub>2</sub>O system were developed for a constant temperature and partial  $\text{CO}_2$  pressure (i.e. constant concentration of dissolved  $\text{CO}_2$ ). The starting point was the open literature data/diagrams for a simpler Fe-H<sub>2</sub>O system at elevated temperatures.<sup>17</sup> Subsequently, additional species were introduced due to the presence of  $\text{CO}_2$ . In addition, those diagrams were correlated with surface characterization of  $\text{CO}_2$  corrosion products formed on mild steel in the temperature range from 25°C to 250°C.

## CONSTRUCTION OF POURBAIX DIAGRAMS FOR AN Fe- $\text{CO}_2$ -H<sub>2</sub>O SYSTEM.

### Thermodynamic Background

Since corrosion is an (electro)chemical process involving reduction/oxidation reactions, it can be described using a thermodynamics framework. An electrochemical reaction is composed of one oxidized species ( $\text{X}^{z+}$ ) and one reduced species (X):



The 1<sup>st</sup> Law of thermodynamics for an isobaric isothermal system can be extended and represented as:

$$\Delta G + zFE = \Delta \tilde{G} \quad (2)$$

Where  $\Delta G$  is the free energy change due to the chemical reaction,  $zFE$  is the electrical energy involved in the process and  $\Delta \tilde{G}$  is the total (electrochemical) free energy for the system. At overall equilibrium, there is no change of total Gibbs energy ( $\Delta \tilde{G} = 0$ ), so we can write:

$$\Delta G = -zFE_{\text{rev}} \quad (3)$$

Where  $E_{rev}$  is called the reversible potential and indicates the reversibility of the electrochemical process at equilibrium.

To calculate  $E_{rev}$ , Equation (3) is substituted into the general expression for Gibbs free energy change of a chemical reaction, Equation (4):

$$\Delta G = \Delta G^\circ + RT \sum_{i=1}^k \ln(c_i)^{n_i} \quad (4)$$

to obtain the well-known Nernst equation, Equation (5):

$$E_{rev} = E_{rev}^\circ - \frac{RT}{zF} \sum_{i=1}^k \ln(c_i)^{n_i} \quad (5)$$

Where  $E_{rev}^\circ$  is the reversible potential as defined at standard conditions using unit concentrations and reference temperature and pressure.

However, the Nernst equation is unable to correct for concentration and temperature simultaneously. To determine the reversible potential of a redox reaction at any temperature,  $E_{rev}^\circ$  is calculated at that temperature, which can be found from the Gibbs energy change,  $\Delta G^\circ$ . For instance, the Gibbs energy change of reaction for the dissolution of iron (Equation [6]), the main anodic reaction in a mild steel corrosion process, is expressed as Equation (7):



$$\Delta G^\circ = G_{Fe}^\circ - G_{Fe^{2+}}^\circ - 2G_{e^-}^\circ \quad (7)$$

The absolute Gibbs energy of electron,  $G_{e^-}^\circ$  described by Kaye and Thompson is also considered, written as Equation (8).<sup>18</sup> By definition of the Nernst equation, the reversible potential at 1 bar of  $H_2$  and 1 Molar of  $[H^+]$  (pH=0.0) is zero at any temperature. From Table 1, the absolute Gibbs energy of  $H^+$  is zero at any temperature.

$$G_{e^-}^\circ = \frac{1}{2} G_{H_2}^\circ \quad (8)$$

The absolute Gibbs energy for each species,  $G^\circ$ , (Equation [9]) at any temperature can be determined using the 1<sup>st</sup> and 2<sup>nd</sup> law of thermodynamics (Equation [10]-[12]):

$$G_{T,P}^\circ = G_{298.15}^\circ + \int_{298.15}^T C_p dT - T \int_{298.15}^T \frac{C_p}{T} dT - \Delta T \cdot S^\circ \quad (9)$$

$$dG = dH - d(TS) \quad (10)$$

$$dH = C_p dT \quad (11)$$

$$dS = \frac{C_p}{T} dT \quad (12)$$

Where  $C_p$  is heat capacity,  $S$  is entropy and  $H$  is enthalpy. In this work, the species considered and their respective thermodynamic data are presented in Table 1.

**Table 1**  
**Thermodynamic Data for the Fe-CO<sub>2</sub>-H<sub>2</sub>O System**

Species	$G_{298K}^{\circ}$	$S_{298K}^{\circ}$	$C_p = a + bT + cT^{-2} + dT^2 + eT^{-0.5}$ (J/mol/K)					Ref.
	(kJ/mol)	(J/mol/K)	a	$b \times 10^3$	$c \times 10^{-6}$	$d \times 10^3$	$e \times 10^{-4}$	
Fe <sub>(s)</sub>	0.0	27.28	28.18	-7.32	-0.290	0.0250	0.0	14
Fe <sup>2+</sup> <sub>(aq)</sub>	-91.88	-105.6	-2.0	0.0	0.0	0.0	0.0	14
Fe(OH) <sub>2(s)</sub>	-491.98	88.0	116.06	8.648	-2.874	0.0	0.0	14
Fe <sub>3</sub> O <sub>4(s)</sub>	-1,012.6	146.14	2659.1	-2521.53	20.734	1.368	-3.646	14
Fe <sup>3+</sup> <sub>(aq)</sub>	-17.8	-276.94	-143	0.0	0.0	0.0	0.0	14
Fe <sub>2</sub> O <sub>3(s)</sub> *	-744.3	87.40	-838.61	-2343.4	0.0	0.605	0.0	14
α-FeO(OH) <sub>(s)</sub>	-485.3	60.4	49.37	83.68	0.0	0.0	0.0	14
Fe(OH) <sub>3(s)</sub>	-705.3	106.7	127.61	41.639	-4.217	0.0	0.0	14
Fe(OH) <sub>2</sub> <sup>+</sup> <sub>(aq)</sub>	-459.50	8.0	230.0	0.0	0.0	0.0	0.0	14
FeCO <sub>3(s)</sub>	-680.3	95.47	257.38	-0.0462	1.523	0.0	-3.082	19
H <sup>+</sup> <sub>(aq)</sub>	0.0	0.0	0.0	0.0	0.0	0.0	0.0	20
OH <sup>-</sup> <sub>(aq)</sub>	-157.2	-10.878	506.77	-1.181	-24.60	0.0	0.0	20
H <sub>2</sub> O <sub>(l)</sub>	-237.1	70.01	20.36	109.2	2.03	0.0	0.0	20
H <sub>2(g)</sub>	0.0	130.7	26.88	3.59	0.11	0.0	0.0	20
O <sub>2(g)</sub>	0	205.1	29.15	6.48	-0.18	-1.02	0.0	20
CO <sub>2(g)</sub>	-394.51	213.8	51.13	4.37	-1.47	0.0	0.0	20

\*  $C_{p(Fe_2O_3)} = a + bT + cT^{-2} + dT^2 + fT^{0.5} + gT^{-1}$  (J/mol/K), where  $f = 86.525$  and  $g = 2.782 \times 10^4$ .

### Equilibria in the Fe-CO<sub>2</sub>-H<sub>2</sub>O System

The equilibrium concentrations of species in a homogenous CO<sub>2</sub>-H<sub>2</sub>O system can be calculated by simultaneously solving the equations shown in Table 2. Since these chemical reactions are linked via the common species (such as for example H<sup>+</sup>) changing any one concentration will shift the equilibrium concentration for all others. For example, the concentrations of HCO<sub>3</sub><sup>-</sup> and CO<sub>3</sub><sup>2-</sup> are dependent on pH, pCO<sub>2</sub> and of course temperature (which affects the equilibrium constants). When one includes dissolved iron species into the picture, one other heterogeneous chemical reaction needs to be considered here: the formation of solid ferrous carbonate (FeCO<sub>3</sub>). The various ways to represent this chemical reaction in a CO<sub>2</sub>-H<sub>2</sub>O system are shown in Table 3. They are all thermodynamically equivalent, what can be easily shown by combining any one of the reactions from Table 3 with selected reactions shown in Table 2, to get any other reaction in Table 3. Therefore, only one form on the heterogeneous ferrous carbonate formation reaction shown in Table 3 can be used in conjunction with the homogenous chemical reactions listed in Table 2. Finally we can add in the key electrochemical (reduction/oxidation or redox) reactions possible in a Fe-CO<sub>2</sub>-H<sub>2</sub>O system and arrive at the complete list of equilibrium reactions considered in constructing of the Pourbaix diagrams.

**Table 2**  
**Chemical Reactions and Equilibrium Constants for a CO<sub>2</sub>-H<sub>2</sub>O System**

Name	Reaction	Equilibrium Constant
Dissolution of CO <sub>2</sub>	$CO_{2(g)} \rightleftharpoons CO_{2(aq)}$	$H = \frac{C_{CO_2}}{P_{CO_2}}$
CO <sub>2</sub> hydration	$CO_{2(aq)} + H_2O_{(l)} \rightleftharpoons H_2CO_{3(aq)}$	$K_{hyd} = \frac{C_{H_2CO_3}}{C_{CO_2}}$
Carbonic acid dissociation	$H_2CO_{3(aq)} \rightleftharpoons H_{(aq)}^+ + HCO_{3(aq)}^-$	$K_{a1} = \frac{C_{HCO_3^-} C_{H^+}}{C_{H_2CO_3}}$
Bicarbonate anion dissociation	$HCO_{3(aq)}^- \rightleftharpoons H_{(aq)}^+ + CO_{3(aq)}^{2-}$	$K_{a2} = \frac{C_{CO_3^{2-}} C_{H^+}}{C_{HCO_3^-}}$

**Table 3**  
**Examples of the Reactions Representing FeCO<sub>3</sub> Precipitation**

Reaction	Equilibrium Constant
$FeCO_{3(s)} + 2H_{(aq)}^+ \rightleftharpoons Fe_{(aq)}^{2+} + CO_{2(g)} + H_2O_{(l)}$	$K_{sp1} = \frac{P_{CO_2} C_{Fe^{2+}}}{C_{H^+}^2}$
$FeCO_{3(s)} + 2H_{(aq)}^+ \rightleftharpoons Fe_{(aq)}^{2+} + H_2CO_{3(aq)}$	$K_{sp2} = \frac{C_{H_2CO_3} C_{Fe^{2+}}}{C_{H^+}^2}$
$FeCO_{3(s)} + H_{(aq)}^+ \rightleftharpoons Fe_{(aq)}^{2+} + HCO_{3(aq)}^-$	$K_{sp3} = \frac{C_{HCO_3^-} C_{Fe^{2+}}}{C_{H^+}}$
$FeCO_{3(s)} \rightleftharpoons Fe_{(aq)}^{2+} + CO_{3(aq)}^{2-}$	$K_{sp4} = C_{CO_3^{2-}} C_{Fe^{2+}}$

## Pourbaix Diagrams

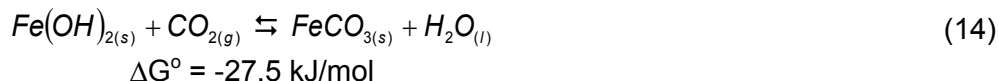
All the reactions, chemical and electrochemical, considered in the present study are listed in Table 4, along with the oxygen and hydrogen reactions. To construct a Pourbaix diagram, the Nernst equation is used for electrochemical reactions, and simple equilibrium expressions are used for the chemical reaction. In the third column, the Nernst expression for the reversible potential is given for the electrochemical reactions while the equilibrium pH is shown for the chemical reactions.

For example, at the reversible potential for iron deposition/dissolution (Reaction no. 1 in Table 4), the reaction is in equilibrium and no corrosion or loss of Fe<sup>2+</sup> is occurring. However, if the potential is higher than the reversible potential of this reaction, then reaction no. 1 proceeds from right to left more than left to right and iron corrodes. In contrast, if the potential is lower than the reversible potential of this reaction, then reaction no. 1 proceeds from left to right and deposits iron in a reduction reaction.

An example of a Pourbaix diagram for an Fe-H<sub>2</sub>O system at 25°C was generated using thermodynamic data given in Table 1 and is shown in Figure 1. The lines *H* and *O* correspond to the equilibrium redox potential of hydrogen and oxygen evolution, respectively. Where the stable state of iron is ferrous ion, Fe<sup>2+</sup>, (the area under the line *H* and above the Fe boundary) in deaerated acidic, neutral, or mildly alkaline conditions, spontaneous corrosion of steel will occur. For higher pH, the layer of solid Fe(OH)<sub>2</sub> or Fe<sub>3</sub>O<sub>4</sub> will form on the surface of the steel (the area under the line *H* and above the Fe boundary) which may give some degree of protection from active corrosion.

An example of a Pourbaix diagram for an Fe-CO<sub>2</sub>-H<sub>2</sub>O system at 25°C is shown in Figure 2a. Based on experimental results (described below), 10ppm of Fe<sup>2+</sup> was selected to generate Pourbaix diagram

shown there. In a deaerated acidic condition,  $\text{Fe}^{2+}$  is the most thermodynamically stable state of iron. For mildly acidic and alkaline regions, the dotted lines show that  $\text{FeCO}_3$ ,  $\text{Fe}(\text{OH})_2$  and  $\text{Fe}_3\text{O}_4$  can coexist at approximately the same conditions. However,  $\text{FeCO}_3$  is the most thermodynamically stable species of the three (i.e. it has the lowest free energy). The other two species must therefore be considered as metastable, i.e. they would be transformed into  $\text{FeCO}_3$  eventually. This can be seen by inspection of the thermodynamic data in Table 1, where the standard free energy of formation for  $\text{FeCO}_3$  is more negative than that of for example  $\text{Fe}(\text{OH})_2$ . This means  $\text{Fe}(\text{OH})_2$  is unstable with respect to  $\text{FeCO}_3$ , i.e.  $\text{Fe}(\text{OH})_2$  will eventually convert into  $\text{FeCO}_3$ , via Reaction (14).



The same strategy can also be applied to determine the relative stability of  $\text{FeCO}_3$  vs.  $\text{Fe}_3\text{O}_4$ ; it is found that the former is more stable, i.e. all  $\text{Fe}_3\text{O}_4$  would eventually convert into  $\text{FeCO}_3$ .

Using the same methodology, the diagrams for an Fe-CO<sub>2</sub>-H<sub>2</sub>O system at temperatures of 80, 120, 150, 200 and 250°C are constructed as shown in Figure 2b – Figure 2f. By inspection of these Pourbaix diagrams, two conclusions can be made with respect to the nature of the corrosion product, as a function of pH and temperature:

- As the temperature increases, the solubility line of  $\text{FeCO}_3$  shifts to the left increasing the possibility of precipitation at lower pH. In other words, at higher temperature  $\text{FeCO}_3$  is stable at lower pH.
- At temperatures below 80°C, the stable state of iron in acidic conditions is  $\text{Fe}^{2+}$  and in neutral and alkaline conditions it is  $\text{FeCO}_3$ . As the temperature increases up to 250°C,  $\text{Fe}_3\text{O}_4$  becomes the more stable product in neutral and alkaline conditions.

The generated Pourbaix diagrams were in broad agreement with those reported by Ueda and Nishimura and Kodama for the same conditions.<sup>21-22</sup> New experiments were conducted in the present study to further verify the validity of the constructed Pourbaix diagrams, particularly for higher temperatures (80 – 250°C).

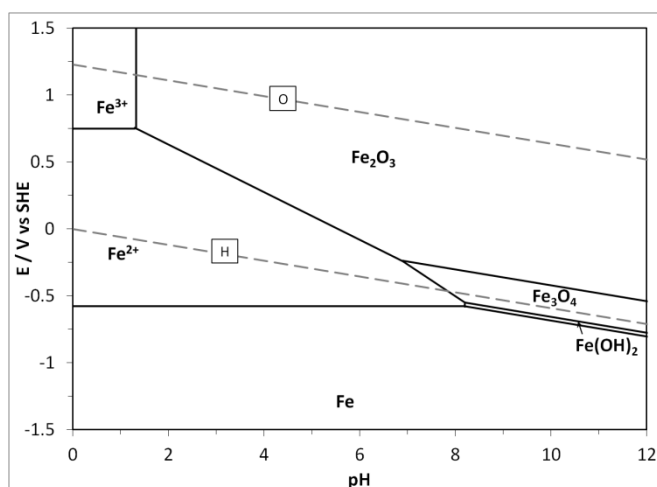
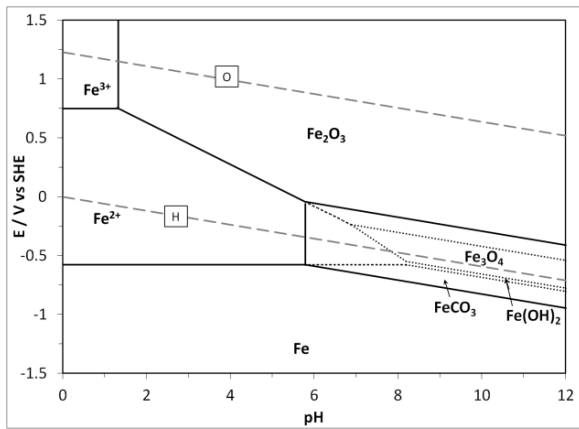


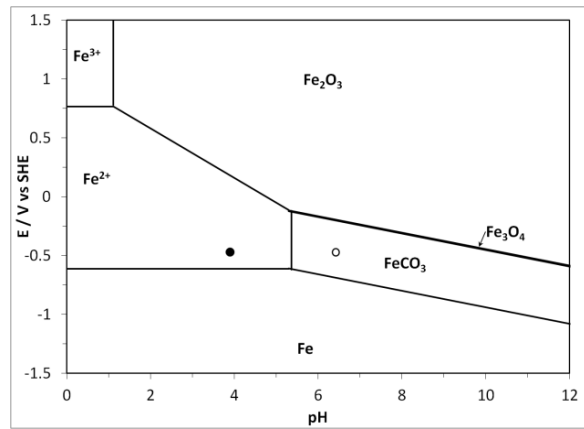
**Figure 1: Example of a Pourbaix diagram for an Fe-H<sub>2</sub>O system at 25°C;  
 $C_{\text{Fe}^{2+}} = 10\text{ppm}$ ,  $C_{\text{Fe}^{3+}} = 10\text{ppm}$ ,  $P_{\text{H}_2} = 1\text{bar}$ ,  $P_{\text{O}_2} = 1\text{bar}$ .**

**Table 4**  
**Key Reactions Considered in the Pourbaix Diagrams for Iron along with the Expressions for their Equilibrium (Reversible) Potential or pH.**

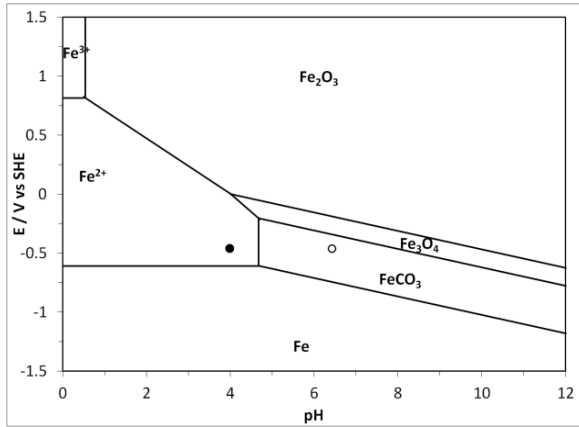
No.	Reaction	Equilibrium Potential in V or pH
H	$2H_2O + 2e^- \rightleftharpoons H_2 + 2OH^-$	$E_{rev(H^+/H_2)} = \frac{RT}{2F} \ln \left( \frac{c_{H^+}^2}{p_{H_2}} \right)$
O	$O_2 + 4H^+ + 4e^- \rightleftharpoons 2H_2O$	$E_{rev(O_2/H_2O)} = E_{rev(O_2/H_2O)}^o + \frac{RT}{4F} \ln(p_{O_2} c_{H^+}^4)$
1.	$Fe^{2+} + 2e^- \rightleftharpoons Fe$	$E_{rev(Fe^{2+}/Fe)} = E_{rev(Fe^{2+}/Fe)}^o + \frac{RT}{2F} \ln(c_{Fe^{2+}})$
2.	$Fe^{3+} + e^- \rightleftharpoons Fe^{2+}$	$E_{rev(Fe^{3+}/Fe^{2+})} = E_{rev(Fe^{3+}/Fe^{2+})}^o - \frac{RT}{F} \ln \left( \frac{c_{Fe^{2+}}}{c_{Fe^{3+}}} \right)$
3.	$Fe^{2+} + 2H_2O \rightleftharpoons Fe(OH)_2 + 2H^+$	$pH_{Fe^{2+}/Fe(OH)_2} = -\log \left( K_{Fe^{2+}/Fe(OH)_2} c_{Fe^{2+}} \right)^{\frac{1}{2}}$
4.	$Fe(OH)_2 + 2H^+ + 2e^- \rightleftharpoons Fe + 2H_2O$	$E_{rev(Fe(OH)_2/Fe)} = E_{rev(Fe(OH)_2/Fe)}^o + \frac{RT}{2F} \ln(c_{H^+})^2$
5.	$Fe_3O_4 + 2H_2O + 2H^+ + 2e^- \rightleftharpoons 3Fe(OH)_2$	$E_{rev(Fe_3O_4/Fe(OH)_2)} = E_{rev(Fe_3O_4/Fe(OH)_2)}^o + \frac{RT}{2F} \ln(c_{H^+})^2$
6.	$6Fe_2O_3 + 4H^+ + 4e^- \rightleftharpoons 4Fe_3O_4 + 2H_2O$	$E_{rev(Fe_2O_3/Fe_3O_4)} = E_{rev(Fe_3O_4/Fe_2O_3)}^o + \frac{RT}{4F} \ln(c_{H^+})^4$
7.	$Fe_3O_4 + 8H^+ + 2e^- \rightleftharpoons 3Fe^{2+} + 4H_2O$	$E_{rev(Fe_3O_4/Fe^{2+})} = E_{rev(Fe_3O_4/Fe^{2+})}^o - \frac{RT}{2F} \ln \left( \frac{c_{Fe^{2+}}^3}{c_{H^+}^8} \right)$
8.	$2Fe_2O_3 + 12H^+ + 4e^- \rightleftharpoons 4Fe^{2+} + 6H_2O$	$E_{rev(Fe_2O_3/Fe^{2+})} = E_{rev(Fe_2O_3/Fe^{2+})}^o - \frac{RT}{4F} \ln \left( \frac{c_{Fe^{2+}}^4}{c_{H^+}^{12}} \right)$
9.	$Fe_3O_4 + 8H^+ + 8e^- \rightleftharpoons 3Fe + 4H_2O$	$E_{rev(Fe_3O_4/Fe)} = E_{rev(Fe_3O_4/Fe)}^o + \frac{RT}{8F} \ln(c_{H^+}^8)$
10.	$2Fe^{3+} + 3H_2O \rightleftharpoons Fe_2O_3 + 6H^+$	$pH_{(Fe^{3+}/Fe_2O_3)} = -\log \left( K_{(Fe^{3+}/Fe_2O_3)} c_{Fe^{3+}}^2 \right)^{\frac{1}{6}}$
11.	$Fe^{2+} + CO_{2(g)} + H_2O \rightleftharpoons FeCO_3 + 2H^+$	$pH_{(Fe^{2+}/FeCO_3)} = -\log \left( K_{(Fe^{2+}/FeCO_3)} c_{Fe^{2+}} p_{CO_2} \right)^{\frac{1}{2}}$
12.	$Fe_3O_4 + 3CO_{2(g)} + 2H^+ + 2e^- \rightleftharpoons 3FeCO_3 + H_2O$	$E_{rev(Fe_3O_4/FeCO_3)} = E_{rev(Fe_3O_4/FeCO_3)}^o + \frac{RT}{2F} \ln(c_{H^+}^2 p_{CO_2}^3)$
13.	$FeCO_3 + 2H^+ + 2e^- \rightleftharpoons Fe + CO_{2(g)} + H_2O$	$E_{rev(FeCO_3/Fe)} = E_{rev(FeCO_3/Fe)}^o - \frac{RT}{2F} \ln \left( \frac{p_{CO_2}}{c_{H^+}^2} \right)$
14.	$Fe_2O_3 + 2H^+ + 2CO_2 + 2e^- \rightleftharpoons 2FeCO_3 + H_2O$	$E_{rev(Fe_2O_3/FeCO_3)} = E_{rev(Fe_2O_3/FeCO_3)}^o + \frac{RT}{2F} \ln(c_{H^+}^2 p_{CO_2}^2)$



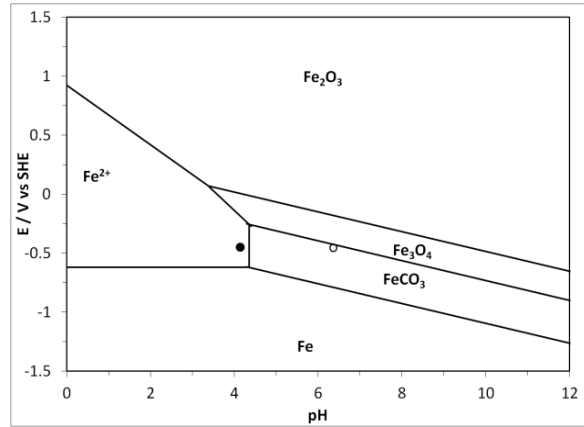
a. 25°C



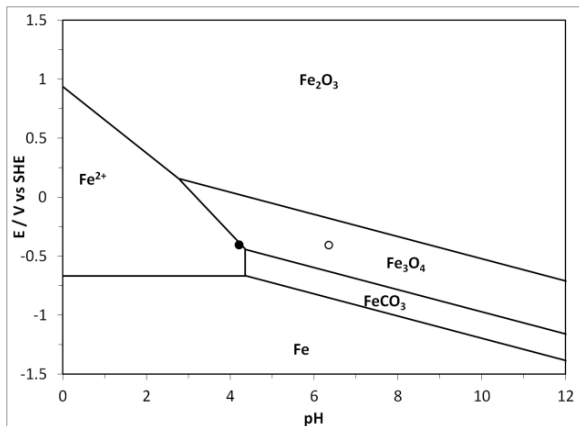
b. 80°C



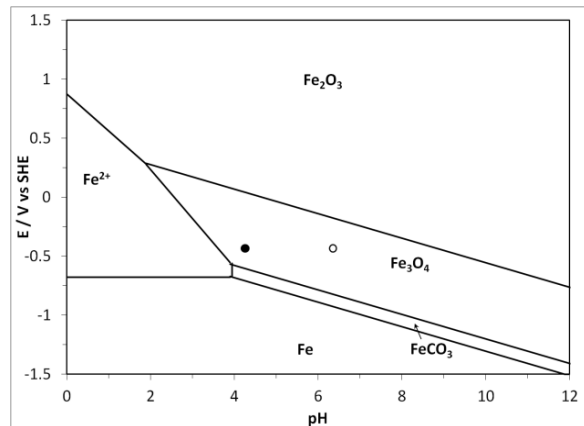
c. 120°C



d. 150°C



e. 200°C



f. 250°C

**Figure 2: Generated Pourbaix diagrams for Fe-CO<sub>2</sub>-H<sub>2</sub>O systems corresponding to the experimental conditions given in Table 5; C<sub>Fe<sup>2+</sup></sub> = 10ppm, C<sub>Fe<sup>3+</sup></sub> = 10ppm, P<sub>H<sub>2</sub></sub> = 1bar, P<sub>O<sub>2</sub></sub> = 1bar, (symbols: • - bulk pH, ○ - surface pH).**

## EXPERIMENTAL

Experiments were conducted in a 1-liter static S31600 autoclave, which is a closed (constant inventory) system. The electrolyte was aqueous solution with 1 wt.% of sodium chloride, saturated with CO<sub>2</sub> at 1

bar total pressure. For each test, API<sup>(1)</sup> 5L X65 metal samples (10 mm x 10 mm x 2 mm) were added to the fully purged solution in the autoclave and the autoclave was sealed at 25°C. Conditions at the beginning of the experiment were: 1 bar of CO<sub>2</sub> at 25°C and pH 3.83. Then the temperature in the autoclave was increased to the desired value. The effect of temperature on partial pressure and dissolved concentration of CO<sub>2</sub> and pH in this closed system is listed in Table 5. Those data were calculated using equilibrium constants listed in Nordsveen, *et al.*<sup>23</sup> Due to CO<sub>2</sub> solubility, partial pressure of CO<sub>2</sub> and pH increased whereas the concentration of dissolved CO<sub>2</sub> decreased with temperature. At the end of the test (which lasted 1 to 30 days), the temperature was lowered to 80°C and the samples were removed with special care. In order to remove salt from the surface and avoid oxidation of the sample surface, the samples were immediately rinsed with deoxygenated, deionized water and isopropanol, and then dried in an N<sub>2</sub> atmosphere. Sample surfaces were characterized by using scanning electron microscopy (SEM), energy dispersive X-ray spectroscopy (EDX) and X-ray diffraction (XRD). Then, the corrosion product layer formed on the steel surface was removed by immersing the specimens into Clarke solution to determine the weight loss and calculate the corrosion rate.<sup>24</sup> In addition, concentration of Fe<sup>2+</sup> in the solution was measured after each experiment.

**Table 5**  
**Effect of Temperature on P<sub>CO<sub>2</sub></sub> and CO<sub>2</sub> Solubility; Initial Condition=1 bar of CO<sub>2</sub> at 25°C.**

Temperature (°C)	P <sub>CO<sub>2</sub></sub> (Bar)	C <sub>CO<sub>2(aq)</sub></sub> (Molar)	Bulk pH
25	1.00	0.030	3.84
80	1.78	0.025	3.92
120	2.27	0.023	4.02
150	2.54	0.022	4.11
200	2.71	0.023	4.30
250	2.43	0.027	4.52

## RESULTS AND DISCUSSION

### Surface Characterization

#### A change of corrosion products over a range of 80-250°C for 4-day exposure

Scanning electron microscopy (SEM) and X-ray diffraction (XRD) results for the experimental conditions at 80, 120, 150, 200, and 250°C are shown in Figure 3 - Figure 7, respectively. These directly correspond to the Pourbaix diagrams illustrated in Figure 2b – Figure 2f. The SEM results show a mixture of plate-like crystals (“plates”) and oblong prismatic-shaped crystals (“prisms”) on the steel surfaces at 80-150°C (Figure 3a - Figure 5a). No obvious crystal morphology was observed on the surfaces of samples exposed at 200°C and 250°C (Figure 6a - Figure 7a). XRD analysis indicated that FeCO<sub>3</sub> and Fe<sub>2</sub>(OH)<sub>2</sub>CO<sub>3</sub> formed on the steel surface at 80-150°C (Figure 3b - Figure 5b). At 200-250°C, the corrosion product is exclusively Fe<sub>3</sub>O<sub>4</sub> (Figure 6b - Figure 7b).

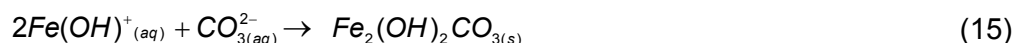
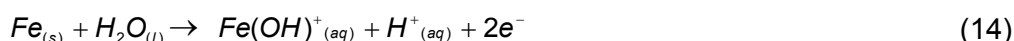
At a first glance, there seems to be a discrepancy between the experimental results and those suggested by the Pourbaix diagrams constructed for the same system, particularly at lower temperature. Using the typical open circuit potential for this Fe-CO<sub>2</sub>-H<sub>2</sub>O system (approximately -0.7 V vs. Ag/AgCl reference electrode or -0.5 V vs. H<sub>2</sub> electrode), and the calculated bulk pH, the operating point can be plotted in the Pourbaix diagram for the purposes of comparison (solid circles on Figure 2b – Figure 2f). With the bulk solution at approximately pH 4, the dominant species in the range 80-150°C should be Fe<sup>2+</sup>, according to the Pourbaix diagram. However, the surface analysis has indicated the

<sup>(1)</sup> American Petroleum Institute, 1220 L Street, NW Washington, DC 20005-4070

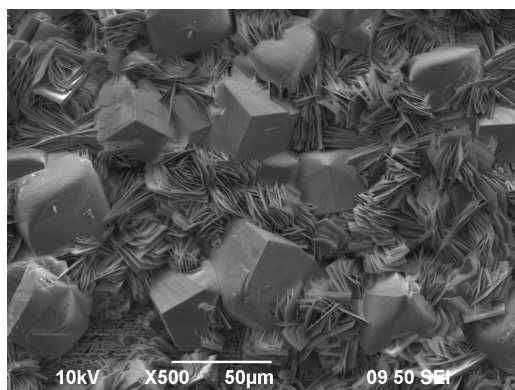
presence of  $\text{FeCO}_3$  and  $\text{Fe}_2(\text{OH})_2\text{CO}_3$ . At  $250^\circ\text{C}$  the Pourbaix diagram suggested that  $\text{Fe}_3\text{O}_4$  is the most stable iron species and the surface analysis confirmed that.

This apparent disagreement can be resolved by accounting for the higher pH at the corroding steel surface, compared to the bulk. According to Han, *et al.*, when the bulk solution is pH 4.0, the pH near a mild steel corroding surface can be as high as pH 6.2.<sup>25</sup> If now this surface pH is used in the Pourbaix diagrams (as hollow circles), it can be seen that from  $80\text{--}150^\circ\text{C}$   $\text{FeCO}_3$  will be the main species expected, while  $\text{Fe}_3\text{O}_4$  will be the most dominant compound from  $200\text{--}250^\circ\text{C}$ . Taking into account the surface pH, the experimental results agree with those predicted with the Pourbaix diagrams, and the latter can be considered validated.

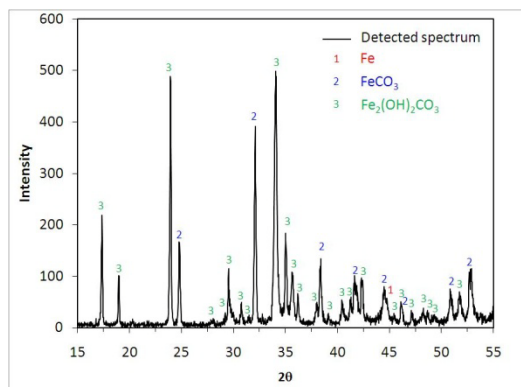
To elaborate on the corrosion products observed.  $\text{FeCO}_3$  and  $\text{Fe}_2(\text{OH})_2\text{CO}_3$  were observed in all experiments below  $200^\circ\text{C}$ . However,  $\text{Fe}_2(\text{OH})_2\text{CO}_3$  was not considered in the Pourbaix diagram construction as it is considered to be an intermediate, metastable species, leading to formation of  $\text{FeCO}_3$  via the following multistep mechanism:<sup>26-29</sup>



To confirm this scenario, variable length experiments were conducted at  $120^\circ\text{C}$ , and are described in the following section.

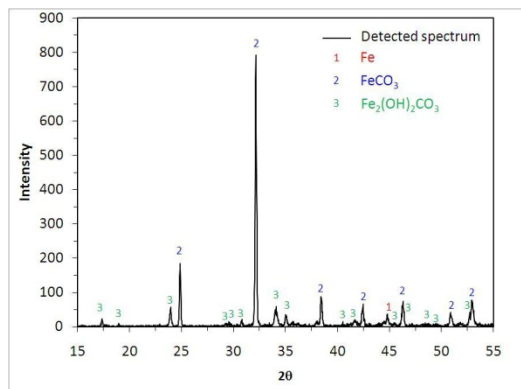
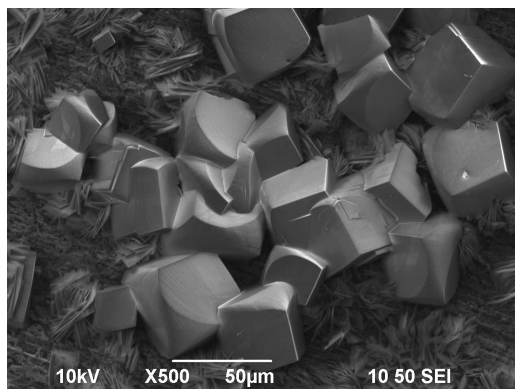


a. SEM image



b. XRD analysis

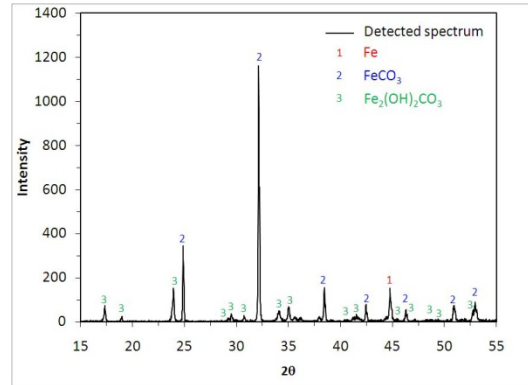
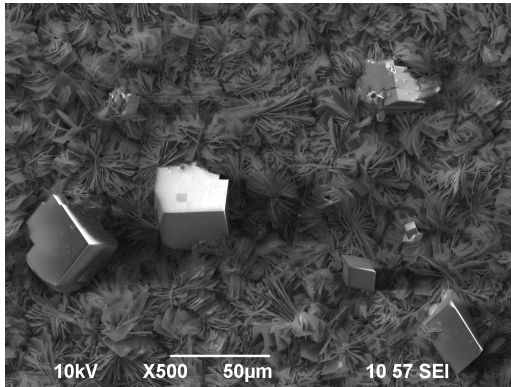
**Figure 3: Corrosion product layer at  $80^\circ\text{C}$ , 4 days**



a. SEM image

b. XRD analysis

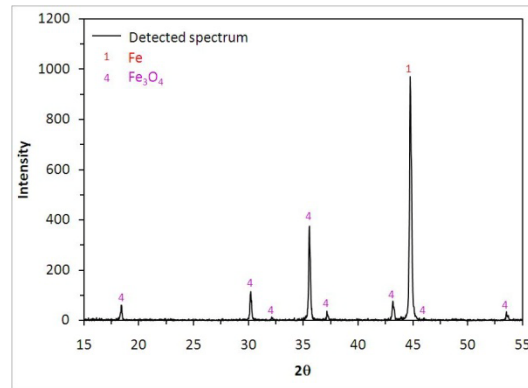
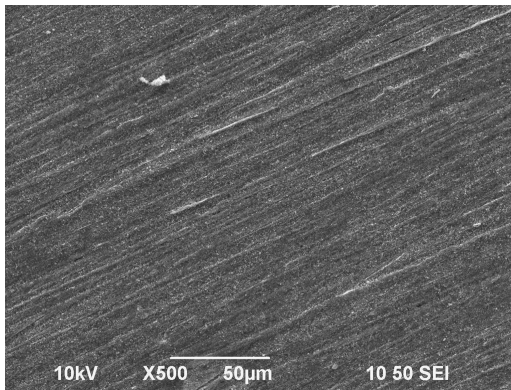
**Figure 4: Corrosion product layer at 120°C, 4 days**



a. SEM image

b. XRD analysis

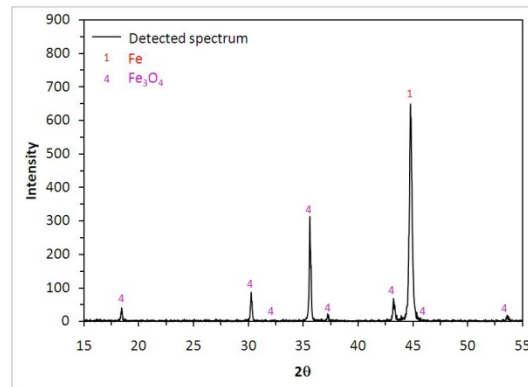
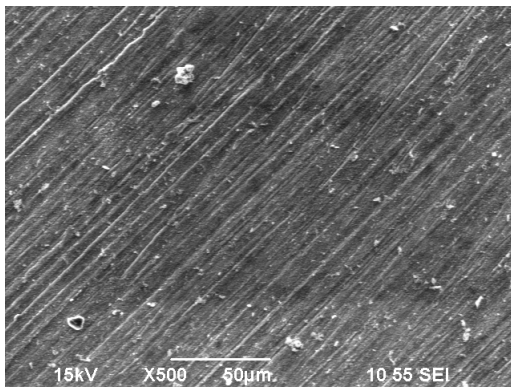
**Figure 5: Corrosion product layer at 150°C, 4 days**



a. SEM image

b. XRD analysis

**Figure 6: Corrosion product layer at 200°C, 4 days**



a. SEM image

b. XRD analysis

**Figure 7: Corrosion product layer at 250°C, 4 days**

A change of corrosion products with time at 120°C

Since Fe<sub>2</sub>(OH)<sub>2</sub>CO<sub>3</sub> was observed as a dominant corrosion product in abovementioned experiments at 120°C, a progression of tests lasting 1 – 30 days was performed to determine the kinetics of the suggested transformation of Fe<sub>2</sub>(OH)<sub>2</sub>CO<sub>3</sub> into FeCO<sub>3</sub>. The SEM images and XRD analysis for 1, 2, 4, 10, and 30 day tests at 120°C confirm that the transformation of Fe<sub>2</sub>(OH)<sub>2</sub>CO<sub>3</sub> into FeCO<sub>3</sub> is occurring.

Figure 8a shows the corrosion product layer on the steel surface after 1 day. The SEM image shows that the steel surface was partially covered by a mixture of thin plates and oblong prisms with an average size of approximately 15  $\mu\text{m}$ . From the XRD analysis, the detected spectrum (Figure 8b) suggest the presence of  $\text{Fe}_2(\text{OH})_2\text{CO}_3$  with small amounts of  $\text{FeCO}_3$ .

After 2 days (Figure 9) and 4 days (Figure 4) of exposure time, there were more crystals formed on the steel surface and the size of prisms was larger than those observed after a 1-day test. The average size of the prisms was 28 and 39  $\mu\text{m}$ , respectively. In addition, it was confirmed by XRD analysis that the plates and prisms were  $\text{Fe}_2(\text{OH})_2\text{CO}_3$  and  $\text{FeCO}_3$  in which the ratios of  $\text{Fe}_2(\text{OH})_2\text{CO}_3$  to  $\text{FeCO}_3$  were 1.67 and 0.13 for the 2-day and 4-day exposure time, respectively.

Similarly, there were morphological mixtures of plates and prisms thoroughly covering the steel surfaces after 10 days of exposure as illustrated in Figure 10a. The average size of the prisms was 50  $\mu\text{m}$ . In contrast to the previous three experiments, only  $\text{FeCO}_3$  was detected by XRD analysis (Figure 10 b).

After 30 days of exposure, the SEM image and XRD pattern (Figure 11) demonstrated only intergrown prisms of  $\text{FeCO}_3$  formed on the steel surface. Therefore, it is concluded that all the plate-shaped crystals were transformed to the prisms during the 30-day exposure. These experiments have confirmed that the  $\text{Fe}_2(\text{OH})_2\text{CO}_3$  was a transition state in forming  $\text{FeCO}_3$ .

Referring back to the generated Pourbaix diagram (Figure 2c) and taking into consideration the surface pH, it is concluded that the expected corrosion product at 120°C is  $\text{FeCO}_3$ . Although  $\text{FeCO}_3$  and  $\text{Fe}_2(\text{OH})_2\text{CO}_3$  were both observed after the 4 day experiments,  $\text{FeCO}_3$  was the only thermodynamically favored corrosion product after 10 and 30 days. Thus, the result from the Pourbaix diagram agrees with the experimental observations.

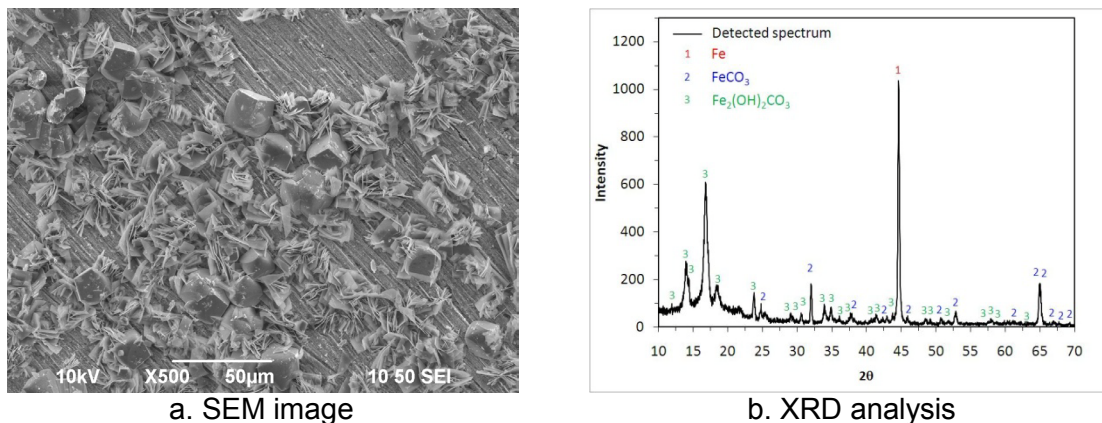
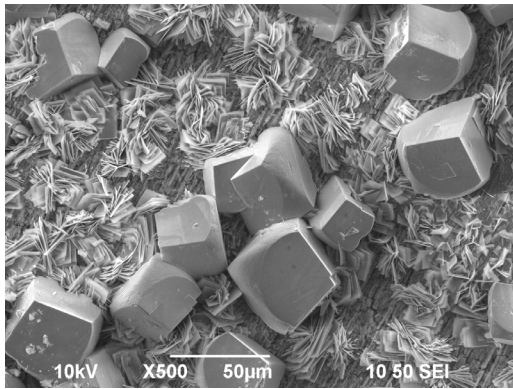
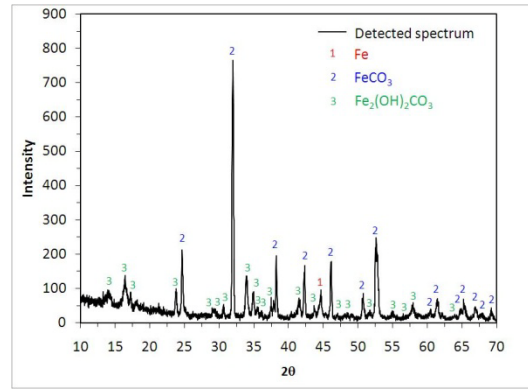


**Figure 8: Corrosion product layer at 120°C, exposure for 1 day.**

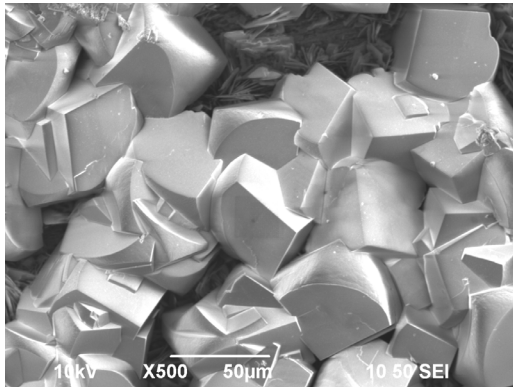


a. SEM image

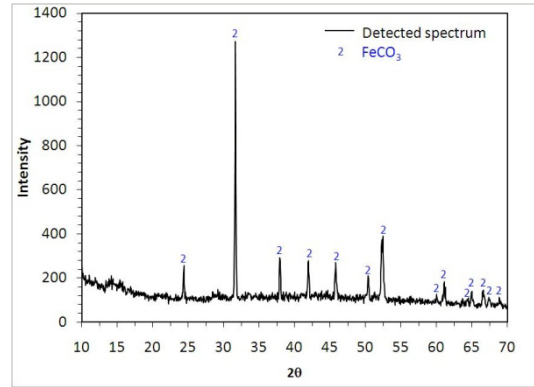


b. XRD analysis

**Figure 9: Corrosion product layer at 120°C, exposure for 2 days.**

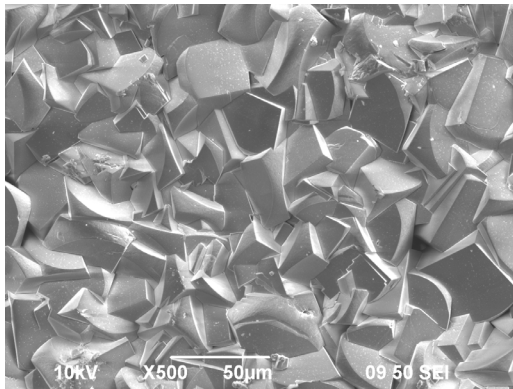


a. SEM image

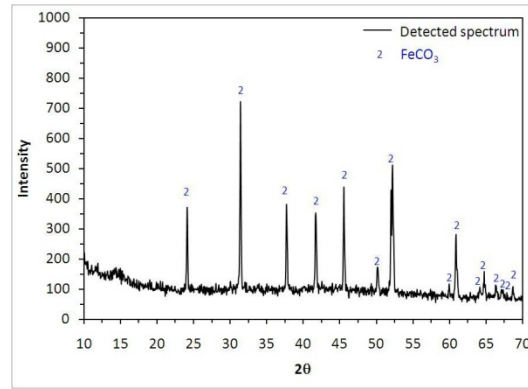


b. XRD analysis

**Figure 10: Corrosion product layer at 120°C, exposure for 10 days.**



a. SEM image



b. XRD analysis

**Figure 11: Corrosion product layer at 120°C, exposure for 30 days.**

## Corrosion Rates

### Corrosion rates over a range of 80-250°C in 4-day exposure

The weight loss corrosion rates are shown in Figure 12. In experimentation from 80°C to 120°C, the corrosion rates increased with temperature. However, the corrosion rates decreased at temperatures above 120°C due to the formation of a protective layer. Ikeda, *et al.* obtained a similar corrosion behavior as the maximum corrosion rate was achieved between 100°C and 150°C.

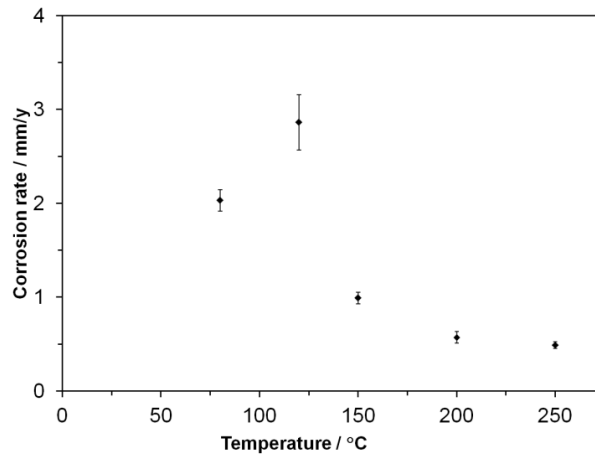


**Figure 12: Weight loss corrosion rate for 4-day exposure.**  
Corrosion rates evolution with time at 120°C

Figure 13 shows the weight loss corrosion rates at 120°C. In experimentation at 120°C, the corrosion rates decreased with time due to the fact that the protective layer formed more thoroughly on the steel surface.

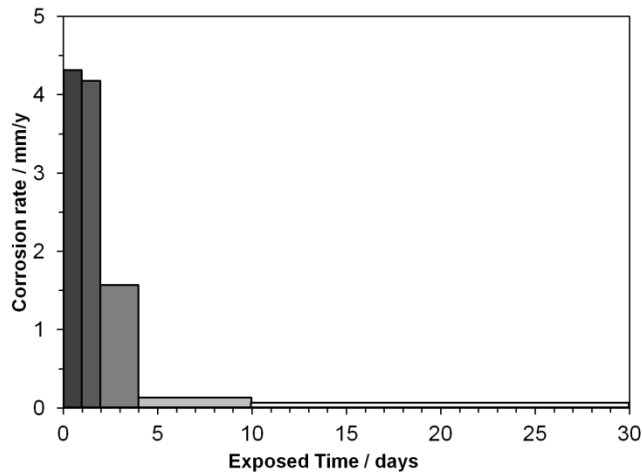


**Figure 13: Weight loss corrosion rate at 120°C**

## CONCLUSIONS

- Pourbaix diagrams for an Fe-CO<sub>2</sub>-H<sub>2</sub>O system at temperatures from 25°C to 250°C were constructed using thermodynamic principles and correlated with surface characterization data for CO<sub>2</sub> corrosion products formed on mild steel.
- In 4-day experiments, FeCO<sub>3</sub> and Fe<sub>2</sub>(OH)<sub>2</sub>CO<sub>3</sub> were observed as dominant corrosion products at 80-150°C whereas Fe<sub>3</sub>O<sub>4</sub> was detected at 200-250°C.
- In longer exposures, Fe<sub>2</sub>(OH)<sub>2</sub>CO<sub>3</sub> transformed into FeCO<sub>3</sub>, consistent with the predicted thermodynamic stability.
- Considering surface pH effects, the generated Pourbaix diagrams were validated by experimental results.
- Maximum weight loss corrosion rates were observed at 120°C.

## ACKNOWLEDGEMENTS

The authors would like to thank the following companies for their financial support: BG Group, BP, Champion Technologies, Chevron, Clariant Oil Services, ConocoPhillips, Encana, ENI S.P.A., ExxonMobil, WGIM, NALCO Energy Services, Occidental Oil Company, Petrobras, PETRONAS, PTT, Saudi Aramco, INPEX Corporation, Total, TransCanada. The authors also thank the Center for Electrochemical Engineering Research (CEER), Department of Chemical and Biomolecular Engineering, Ohio University, for the use of the XRD equipment.

## REFERENCES

1. S. Nestic, "Key issues related to modeling of internal corrosion of oil and gas pipelines – A review," *Corrosion Science*, 49 (2007), p. 4308-4338.
2. A. Ikeda, M. Ueda, S. Mukai, "CO<sub>2</sub> corrosion behavior and mechanism of carbon steel and alloy steel," CORROSION/83, paper no. 45, (Houston, TX: NACE, 1983).
3. L. G. S. Gray, B. G. Anderson, M. J. Danysh, P. R. Tremaine, "Effect of pH and temperature on the mechanism of carbon steel corrosion by aqueous carbon dioxide," CORROSION/90, Paper no. 40, (Houston, TX: NACE, 1990).
4. S. Al-Hassan, B. Mishra, D. L. Olson, M. M. Salama, "Effect of microstructure on corrosion of steels in aqueous solutions containing carbon dioxide," *Corrosion*, 54 (1998), p. 480-491.
5. X. Guo, "The effect of corrosion product layers on the anodic and cathodic reactions of carbon steel in CO<sub>2</sub>-saturated MDEA solutions at 100°C," *Corrosion Science*, 41 (1999), p. 1391-1402.
6. G. Lin, M. Zheng, Z. Bai, X. Zhao, "Effect of temperature and pressure on the morphology of carbon dioxide corrosion scales," *Corrosion*, 62 (2006), p. 501-507.
7. A. Ikeda, "Prevention of CO<sub>2</sub> Corrosion of line pipe and oil country tubular goods," CORROSION/84, Paper no.289, (Houston, TX: NACE, 1984).
8. Z. F. Yin, Y. R. Feng, W. Z. Zhao, Z. Q. Bai, G. F. Lin, "Effect of temperature on CO<sub>2</sub> corrosion of carbon steel," *Surface and Interface Analysis*, 41 (2009), no. 6, p. 517-523.
9. C. A. Palacios, J. R. Shadley, "Characteristics of corrosion scales on steels in a CO<sub>2</sub>-saturated NaCl brine," *Corrosion*, 47 (1991), p. 122-127.
10. R. De Marco, Z. Jiang, B. Pejdic, E. Poinen, "An in situ synchrotron radiation grazing incidence X-ray diffraction study of carbon dioxide corrosion," *Journal of The Electrochemical Society*, 152 (2005), p. B389-B392.
11. M. Pourbaix, *Atlas of electrochemical equilibria in aqueous solutions*, 2<sup>nd</sup> ed. (Houston, TX: Nace International, 1974), p. 644.
12. P. Paine, "Technical note: Potential-pH diagrams for the Fe-Cl-H<sub>2</sub>O system at 25 to 150°C," *Corrosion*, 46 (1990), p. 19-21.
13. H. Townsend, "Potential-pH diagrams at elevated temperature for the system Fe-H<sub>2</sub>O," *Corrosion Science*, 10 (1970), p. 343-358.
14. B. Beverskog, I. Puigdomenech, "Revised Pourbaix diagrams for iron at 25-300 degrees C," *Corrosion Science*, 38 (1996), p. 2121-2135.
15. M. Pourbaix, "Thermochemical diagrams: Some applications to study of high temperature corrosion," *Materials Science and Engineering*, 87 (1987), p. 303-317.
16. V. Ashworth, P. J. Boden, "Potential-pH diagrams at elevated temperatures," *Corrosion Science*, 10 (1970), p. 709-718.
17. D. C. Silverman, "Presence of solid Fe(OH)<sub>2</sub> in EMF-pH diagram for iron," *Corrosion*, 38 (1982), p. 453-455.
18. M. H. Kaye, W. T. Thompson, "Computation of Pourbaix diagrams at elevated temperature," in R. W. Revie, *Uhlig's Corrosion Handbook*, 3<sup>rd</sup> ed., (Hoboken, NJ: A John Wiley & Sons, Inc., 2011), p. 111-122.
19. R. A. Robie, H. T. Haselton, B. S. Hemingway, "Heat capacities and entropies of rhodochrosite (MnCO<sub>3</sub>) and siderite (FeCO<sub>3</sub>) between 5 and 600 K," *American Mineralogist*, 69 (1984), p. 349-357.

20. O. Knacke, O. Kubaschewski, K. Hesselmann, *Thermochemical properties of inorganic substances*, (Berlin: Springer-Verlag, 1991), p. 2541.
21. M. Ueda, "Potential-pH diagram at elevated temperatures for metal-CO<sub>2</sub>/H<sub>2</sub>S-water systems and the application for corrosion of pure iron," *Corrosion Engineering*, 44 (1995), p. 159-174.
22. J. Dong, T. Nishimura, T. Kodama, "Corrosion behavior of carbon steel in bicarbonate solutions," *Materials Research Society*, 713 (2002), p. 105-112.
23. M. Nordsveen, S. Netic, R. Nyborg, A. Stangeland, "A mechanistic model for carbon dioxide corrosion of mild steel in the presence of protective iron carbonate films – Part 1: Theory and verification," *Corrosion*, 59 (2003), p. 443-456.
24. ASTM<sup>(2)</sup> G1, "Standard Practice for Preparing, Cleaning, and Evaluating Corrosion Test Specimens," (West Conshohocken, PA: ASTM).
25. J. Han, D. Young, H. Colijn, A. Tripathi, S. Netic, "Chemistry and structure of the passive film on mild steel in CO<sub>2</sub> corrosion environments," *Industrial & Engineering Chemistry Research*, 48 (2009), p. 6296-6302.
26. T. R. Lee, R. T. Wilkin, "Iron hydroxy carbonate formation in zerovalent iron permeable reactive barriers: characterization and evaluation of phase stability," *Journal of Contaminant Hydrology*, 116 (2010), p. 47-57.
27. R. De Marco, Z.-T. Jiang, B. Pejic, E. Poinen, "An in situ synchrotron radiation grazing incidence X-Ray diffraction study of carbon dioxide corrosion," *Journal of The Electrochemical Society*, 152 (2005), p. B389-B392.
28. C. Rémazeilles, P. Refait, "Fe(II)hydroxycarbonate Fe<sub>2</sub>(OH)<sub>2</sub>CO<sub>3</sub> (chukanovite) as iron corrosion product: Synthesis and study by Fourier Transform Infrared Spectroscopy," *Polyhedron*, 28 (2009), p. 749-756.
29. M. L. Schlegel, C. Bataillon, C. Blanc, D. Prêt, E. Foy, "Anodic activation of iron corrosion in clay media under water-saturated conditions at 90 degrees C: characterization of the corrosion interface," *Environmental Science & Technology*, 44 (2010), p. 1503-1508.

---

<sup>(2)</sup> ASTM International, 100 Barr Harbor Drive, PO Box C700, West Conshohocken, PA, 19428-2959